AGU PUBLICATIONS

JGR

Journal of Geophysical Research: Solid Earth

RESEARCH ARTICLE
10.1002/2014JB011409

Key Points:
- Multi-interval effect of complex magma pulses
- Aseismic intrusions along/close the CL, energetic intrusions along the KL
- Modeling consistent with CFS predictions and seismicity fluctuations

Correspondence to:
S. C. Stiros,
stiros@upatras.gr

Citation:
Saltogianni, V., S. C. Stiros, A. V. Newman, K. Flanagan, and F. Moschas (2014), Time-space modeling of the dynamics of Santorini volcano (Greece) during the 2011–2012 unrest, *J. Geophys. Res. Solid Earth*, *119*, doi:10.1002/2014JB011409.

Received 24 JUN 2014
Accepted 7 OCT 2014
Accepted article online 12 OCT 2014

Time-space modeling of the dynamics of Santorini volcano (Greece) during the 2011–2012 unrest

Vasso Saltogianni[1], Stathis C. Stiros[1], Andrew V. Newman[2], Kelly Flanagan[2], and Fanis Moschas[1]

[1]Department of Civil Engineering, University of Patras, Patras, Greece, [2]School of Earth and Atmospheric Sciences, Georgia Institute of Technology, Atlanta, Georgia, USA

Abstract The 2011–2012 unrest of Santorini (Thera) volcano (Aegean Sea, Greece) was associated with microseismicity confined to the Kameni Line (KL), a major tectonovolcanic lineament, and has been regarded as a single magmatic episode, produced by a spherical source derived from inversion of GPS data. However, such a source is a few kilometers away from the KL and cannot explain observed microseismicity. For this reason, we divided the unrest episode into five periods based on the fluctuations of seismicity and deformation rates and investigated the connection between seismicity and two spherical magmatic point sources for each period. Based on a new inversion algorithm and consistent GPS data, we recognized during the volcano unrest episode an unstable pattern of intrusions correlating with both the KL and Columbo Line (CL), a second major tectonovolcanic lineament. Intrusions correlating with CL appear relatively persistent, aseismic, small, and shallow, which is consistent with marine geophysical evidence for arrested shallow dykes and geodetic evidence from a previous inflation episode. During the two periods of intense seismicity, sources close to the KL, explaining seismicity, were obtained. This unstable pattern of intrusions explains both the well-observed location and timing of seismicity as well as ground deformation and is consistent with results of an Okada-type inversion for a sill and a dyke. The stress interactions between the two sources agree with Coulomb failure stress models. Santorini appears to be affected by concurrent offset magma pulses, and only recent activity from a magma pulse below the KL produced microseismic swarms.

1. Introduction

After the large Minoan eruption about 3650 years ago, Santorini (Thera) caldera in the Aegean Sea has been marked by frequent smaller eruptions, the last of which occurred between 1928 and 1950 [*Bond and Sparks*, 1976; *Druitt and Francaviglia*, 1992; *McCoy and Heiken*, 2000]. Following 1950, the caldera remained relatively calm until 2010 [*Dimitriadis et al.*, 2005, 2009; *Bohnhoff et al.*, 2006]. The only observed exception was a small-scale, slow and aseismic inflation of the northern part of the caldera between 1994 and 2000 [*Stiros et al.*, 2010; *Saltogianni and Stiros*, 2012a].

During 2011 and 2012 the Santorini caldera showed signs of unrest with swarms of micro-earthquakes (Figure 1) and crustal deformation regarded as the first step toward a potential future eruption [*Blundy and Rust*, 2012; *Newman et al.*, 2012; *Parks et al.*, 2012]. This was primarily because seismicity was confined to a subvertical surface approximately 6 km long and 10 km deep [*Newman et al.*, 2012; *Konstantinou et al.*, 2013], correlating with the Kameni Line, hereafter KL (Figure 1). The latter is the main tectonovolcanic lineament in the Santorini caldera, an extensional fracture in which all the eruptive events after the Minoan eruption have occurred [*Druitt et al.*, 1989; *Pyle*, 1990; *Pyle and Elliott*, 2006].

Concurrently, with the seismic data, permanent and survey GPS data, as well as interferometric synthetic aperture radar data, have shown an approximately radial deformation pattern with cumulative concentric displacement of about 10 cm. This deformation is centered in the middle of the north part of the caldera, located between the KL and the Columbo Line, hereafter CL [*Newman et al.*, 2012; *Parks et al.*, 2012; *Lagios et al.*, 2013], another major tectonovolcanic lineament extending beyond the caldera edifice [*Druitt et al.*, 1989]. Analytic modeling was used to assign the observed deformation to a point source spherical intrusion, called a Mogi source [*Mogi*, 1958] within the northern part of the caldera, about 2 km from the KL (Figure 1) and about 4 km depth [*Newman et al.*, 2012; *Parks et al.*, 2012; *Foumelis et al.*, 2013; *Lagios et al.*, 2013; *Papoutsis et al.*, 2013].

This intrusion has been regarded by most of the above authors as the driving mechanism of the seismicity along the KL during the 2011–2012 unrest [see also *Konstantinou et al.*, 2013]. *Newman et al.* [2012], however,

©2014. American Geophysical Union. All Rights Reserved.

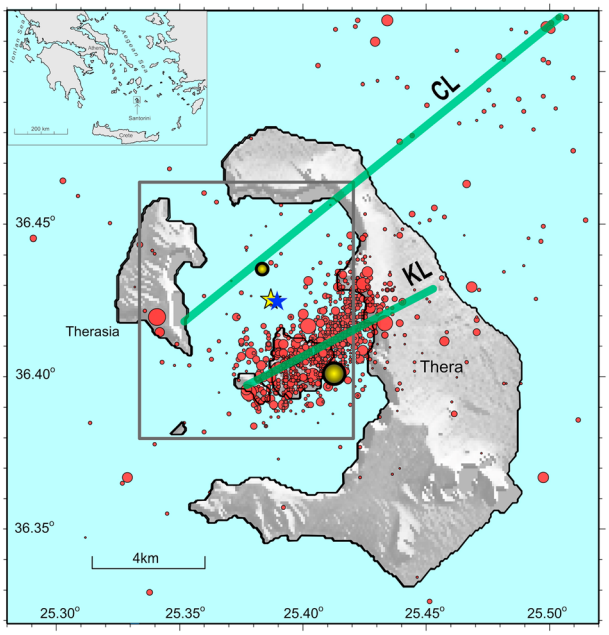

Figure 1. Swarm of small earthquakes (local magnitude ≤3.2) during the 2011–2012 period of unrest (red dots scaled by magnitude, redrafted after *Newman et al.* [2012]). Dot size indicates events with magnitude $M \geq 3.0$, $3 < M < 2$, $2 < M < 1$ $M < 1$. Green lines indicate the Columbo (CL) and Kameni lines (KL), and stars indicate the single spherical magma sources by *Newman et al.* [2012] (blue) and *Parks et al.* [2012] (yellow) which are offset from the KL. Two yellow circles indicate the location of the two sources (double source model of Figure 2), corresponding to the cumulative deformation between August 2011 and July 2013. The boundaries of the grid containing the possible locations of magma sources examined in our analysis are marked by a rectangle (see section 6.2).

identified difficulties in confining all deformation to a single spherical source and tested alternative models, including a distributed sill, to explain both surface deformation and seismicity (see Figure S4 in *Newman et al.* [2012]) and a two-source Mogi model (Figure 2). The implication of these latter models is that a shallow source at the northern part of the caldera may mask the deformation produced by a second, deeper source responsible for the seismicity observed.

The particular aims of this study are to show the following:

1. Any spherical source within the northern part of the caldera is located in a position unfavorable to produce stresses that would explain the observed seismicity along the KL.
2. Between January 2011 and September 2012, variations in seismicity and in the rates of ground deformation are correlated and define five distinct deformation periods (events or phases in the volcanic deformation [see also *Newman et al.*, 2012; *Konstantinou et al.*, 2013]), each of which is modeled independently.
3. The hypothesis of short-duration (up to a few months) complex magma intrusions, modeled by two spherical sources, may well explain variations in the deformation pattern and the seismicity in Santorini [cf. *Sturkell et al.*, 2008; *Galgana et al.*, 2014].
4. The inferred instability in the intrusion pattern is consistent with ideas for magma pulses from depth [*Sigmundsson et al.*, 2010; *Parks et al.*, 2012; *Druitt et al.*, 2012; *Galgana et al.*, 2014] and testifies to a combination of brittle and plastic behavior of the rocks in the Santorini caldera and to a potential of plastically deforming rocks to arrest dikes at shallow depths [*Gudmundsson*, 2006; *Sakellariou et al.*, 2012] (see below section 8).

The overall modeling analysis of single and dual magma sources is primarily based on the recently introduced Topological Inversion (TOPINV) algorithm that has been tested against synthetic data corresponding to the deformation of Santorini volcano [*Saltogianni and Stiros*, 2013b].

2. Structural Constraints to the 2011–2012 Seismicity

The close correlation between deformation and seismicity [*Newman et al.*, 2012] indicates that the 2011–2012 intracaldera seismicity in Santorini was associated with magma intrusions. However, the preliminary hypothesis that this seismicity along the KL is controlled by a magma source at some distance from the middle of this line (Figure 3a) [see also *Konstantinou et al.*, 2013] is unlikely for the following reasons.

First, the inferred single-source intrusion models with a source in the northern part of the caldera (any of the stars in Figure 1) can only produce compressional, not extensional, faulting along the KL (Figure 3b). Still, the focal mechanisms of the major events of this seismicity correspond to normal faulting, or normal/strike slip faulting with an extension axis approximately normal to the Kammeni Line [*Papazachos et al.*, 2012], schematically shown in Figure 3c, in agreement with the existing tectonovolcanic evidence [*Parks et al.*, 2012].

©2014. American Geophysical Union. All Rights Reserved.

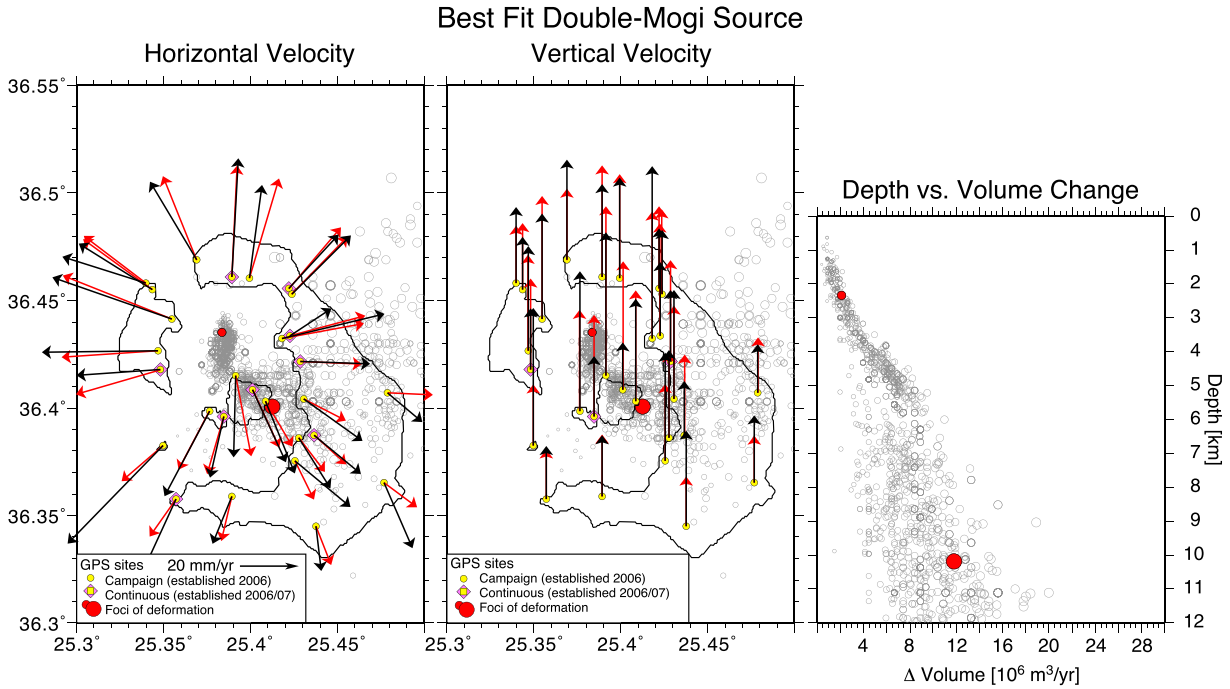

Figure 2. Model of the cumulative deformation of Santorini for the period August 2011 and July 2013 by two Mogi sources solving for eight parameters (*x*,*y*,*z*,d*V*) simultaneously using an 8-D-nested grid search and constrained by 1000 bootstrap runs (grey circles) taking random subsets of the GPS data. (left) Horizontal displacements, (middle) vertical displacements, and (right) depth versus annual rate of volumetric source expansion. Black and red arrows indicate observations and model predictions, respectively. Magma sources are indicated by red circles.

Second, stress σ produced by a magma source with volume V at a distance r is defined by the relationship

$$\sigma \propto Vr^{-3} \tag{1}$$

[*Gudmundsson et al*., 1999; *Gudmundsson*, 2006], indicating a rapid attenuation of stresses away from the source. Based on this relationship, the sources marked by stars in Figure 1 could have only been directly associated with seismicity in their vicinity, and any association with seismicity along KL is rather unlikely. This point is further analyzed on the basis of Coulomb stress changes in section 8.2.

Possible scenarios to explain the observed seismicity are schematically summarized in Figure 4 and cover all possibilities for failure along a fault/seismicity due to changes in principal and shear stresses [*Toda et al*., 2002; *Seebeck and Nicol*, 2009]. Obviously, none of these scenarios are compatible with only one single spherical intrusion source at the northern part of the caldera proposed before (Figure 3a), but it could be consistent with a model of two sources of Figure 2 in which one of the magma sources would correlate with the KL (Figure 4). This justifies a further refinement of the intrusion model during the 2011–2012 unrest.

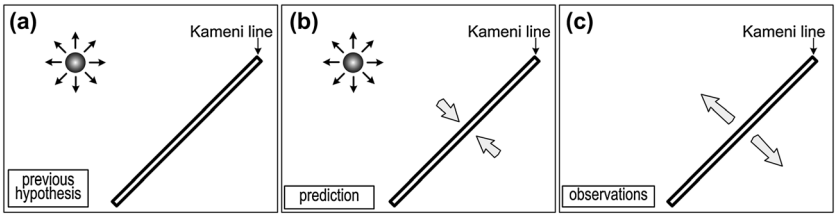

Figure 3. Magma intrusion and seismicity along KL in 2011–2012, a schematic approach in plan view. (a) Location of the magma source relative to KL. (b) Expected stress pattern in KL because of magma pressure (arrows indicating pressure). (c) Inferred stress pattern in KL.

©2014. American Geophysical Union. All Rights Reserved.

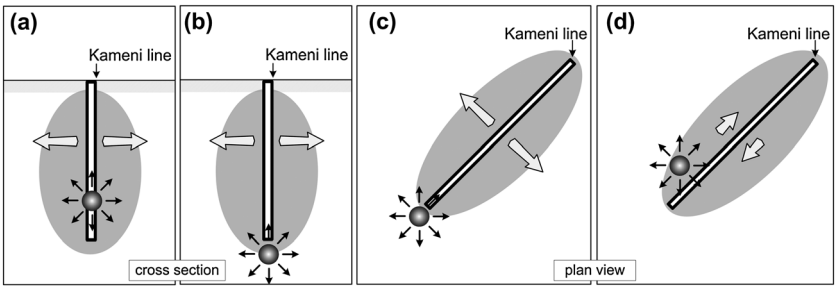

Figure 4. A summary of possible scenarios for the extensional/strike-slip seismicity in the Santorini caldera in 2011–2012 unrest, schematic representation. (a, b) Intrusion inside or just beneath KL (vertical cross section, inspired from *Seebeck and Nicol* [2009]). (c, d) Lateral spreading and shear failure by an intrusion just next to KL (plan view, inspired after *Toda et al.* [2002]).

3. Methodology

Figure 2 can explain the correlation between seismicity and magma intrusion; however, fluctuations in rates of deformation and of seismicity [*Newman et al.*, 2012; *Konstantinou et al.*, 2013] require refined time-dependent modeling. For this reason, our methodology was the following: First, we analyzed the available seismological data of the period 2011–2012 (epicenters and magnitudes) in combination with GPS-derived displacements in order to identify periods of high and low deformation. Second, for each of the periods identified, we tried to model one or two simultaneously active spherical point sources using the available GPS data and the TOPINV software. Third, we analyzed the obtained results in order to understand why and which of the models can explain high and low rates in seismicity and deformation during the specific periods.

Modeling of the intrusion using GPS data was based on the assumption of spherical magma sources (Mogi models), which are described by well-known equations [*Mogi*, 1958] and are valid under certain conditions [*McTigue*, 1987; *Pascal et al.*, 2013]. The overall analysis was based on the TOPINV (Topological Inversion) algorithm, first validated for the adjustment of common geodetic networks and explicitly analyzed in *Saltogianni and Stiros* [2012b, 2013a, 2013b] and in *Stiros and Saltogianni* [2014]. This algorithm permits *simultaneous* inversion of all n unknown variables in a redundant system of highly nonlinear equations for modeling single and double Mogi sources on the basis of a quasi-deterministic approach ("scanning" a n-dimensional grid of all possible values of the unknown variable allowing an error margin) without any need to a priori constrain certain of its components. The algorithm does not lead to point solutions (maxima etc.) but to a set of discrete n-dimensional grid points defining a closed space satisfying the system of equations, and from this space, a stochastic and optimal solution is obtained.

In the Mogi model, any inflation source can be defined by four variables (easting, northing, depth, and volume change) which correspond to a vector (or matrix) $\boldsymbol{x}$ in the R^4 space [*McTigue*, 1987]. The Mogi equations symbolized by f permit to relate this source with the dislocation at a certain surface point; in the case of GPS observations this can be described by a 3-D displacement vector ℓ. Each of the three scalar components of this vector corresponds to an equation that defines the geophysical model [see *Mogi*, 1958; *McTigue*, 1987; *Saltogianni and Stiros*, 2013b].

The equations of the system defining the geophysical model are of the form

$$f_j(x) - \ell_j = v_j \tag{2}$$

where v_j is an unknown error to account for imperfections in the geophysical model f_j and a measurement error of ℓ_j for equation j. Because equations f_j are highly nonlinear, this system cannot be solved (inverted) with conventional methods. The strategy of the TOPINV algorithm is to solve the system of equations on the basis of a priori constraints for the unknowns and of an optimization factor.

Excluding outliers, we may assume that the absolute value of v_j is smaller than a limit $\varepsilon_j > 0$, and we can express ε_j as a product of σ_j with an (unknown) optimization factor k. Hence, from (2) the following inequality is formed

$$\left|f_j - \ell_j\right| < \varepsilon_j \text{ or } \left|f_j - \ell_j\right| < k\sigma_j \tag{3}$$

In the system of equation (3), the unknown errors v_j in measurements have been replaced by k and their standard errors, functioning also as weights. This reduces significantly the number of unknowns. The second

©2014. American Geophysical Union. All Rights Reserved.

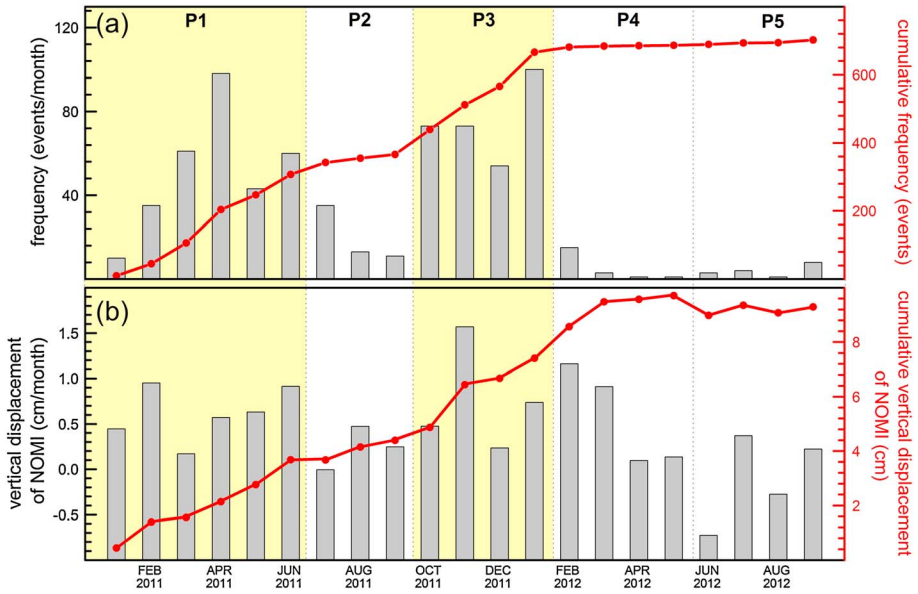

Figure 5. (a) Monthly and cumulative rates of seismicity in Santorini for the unrest period January 2011 to September 2012 ($M_L \geq 1.0$). (b) Monthly and cumulative rates of the vertical movement of GPS station NOMI (see Figure 6) for each of the five periods. The high seismicity and deformation rates of P1 and P3 are highlighted.

step is to define the possible range of each component of the unknown vector (or matrix) $\boldsymbol{x}$ in the R^4 space on the basis of independent constraints (geological, geophysical, etc.) and transform this (continuous) R^4 space to a set of discrete points represented by a four-dimensional grid G, adopting also a spacing between points for each variable (component). The third step is to "scan" all grid points of grid G and identify those which satisfy equation (3) using forward computations and a Boolean logic test (yes/no). At first, a value of $k = 1$ is adopted, and it is tested whether for this value of k it can be defined a set S of grid points, corresponding to a closed space, subset of G. In the case that more than one independent solution exist in G, more than one set of S can be identified. Solution S is then empirically optimized for values of k until the minimum number of grid points for each cluster satisfying the system of equation (3) is obtained; the optimal value of $k = k^*$ corresponds to the optimal set (or sets) S* of grid points. The fourth step is to compute the center of gravity of set (or sets) S* which leads to minimum variance solutions of the unknown vector $\boldsymbol{x}$; such solutions depend only on the initial conditions imposed by grid G and the adopted errors weights of observations. From the calculated center of gravity in the R^4 space (or in the general case in the R^n space for n unknown variables), the full variance covariance matrix of the solution (variances and covariances) is obtained. A mean misfit error can also be quasi-independently obtained from the system of observation equations and the computed solutions.

The overall strategy is not to minimize a certain function but to identify the optimal n-dimensional spaces (clusters of grid points) in which solutions are located. For this reason, the algorithm can identify more than one solution and is not trapped in local minima. The software used is fully efficient for common computers for grids G with a number of grid points of the order of 10^8. In the case of larger grids, either more powerful computers are required or solutions in steps: a larger, coarser grid is first selected and then nested, smaller and finer grids around coarsely identified solutions [*Saltogianni and Stiros*, 2013b].

TOPINV can also be adopted for modeling of the deformation produced by two magma sources [*Saltogianni and Stiros*, 2013b]. In this case, $\boldsymbol{x}$ and grid G are combined in R^8 space whose four-dimensions correspond to each of the two Mogi sources.

4. Periods of Intracaldera Seismicity and Deformation

The Santorini caldera was aseismic for at least the last 10–20 years [*Dimitriadis et al.*, 2005, 2009; *Bohnhoff et al.*, 2006], but between January 2011 and September 2012 about 1000 micro-earthquakes with a maximum magnitude 3.3 occurred along the KL (catalogue of the Seismological Lab of the Thessaloniki University, Greece)

©2014. American Geophysical Union. All Rights Reserved.

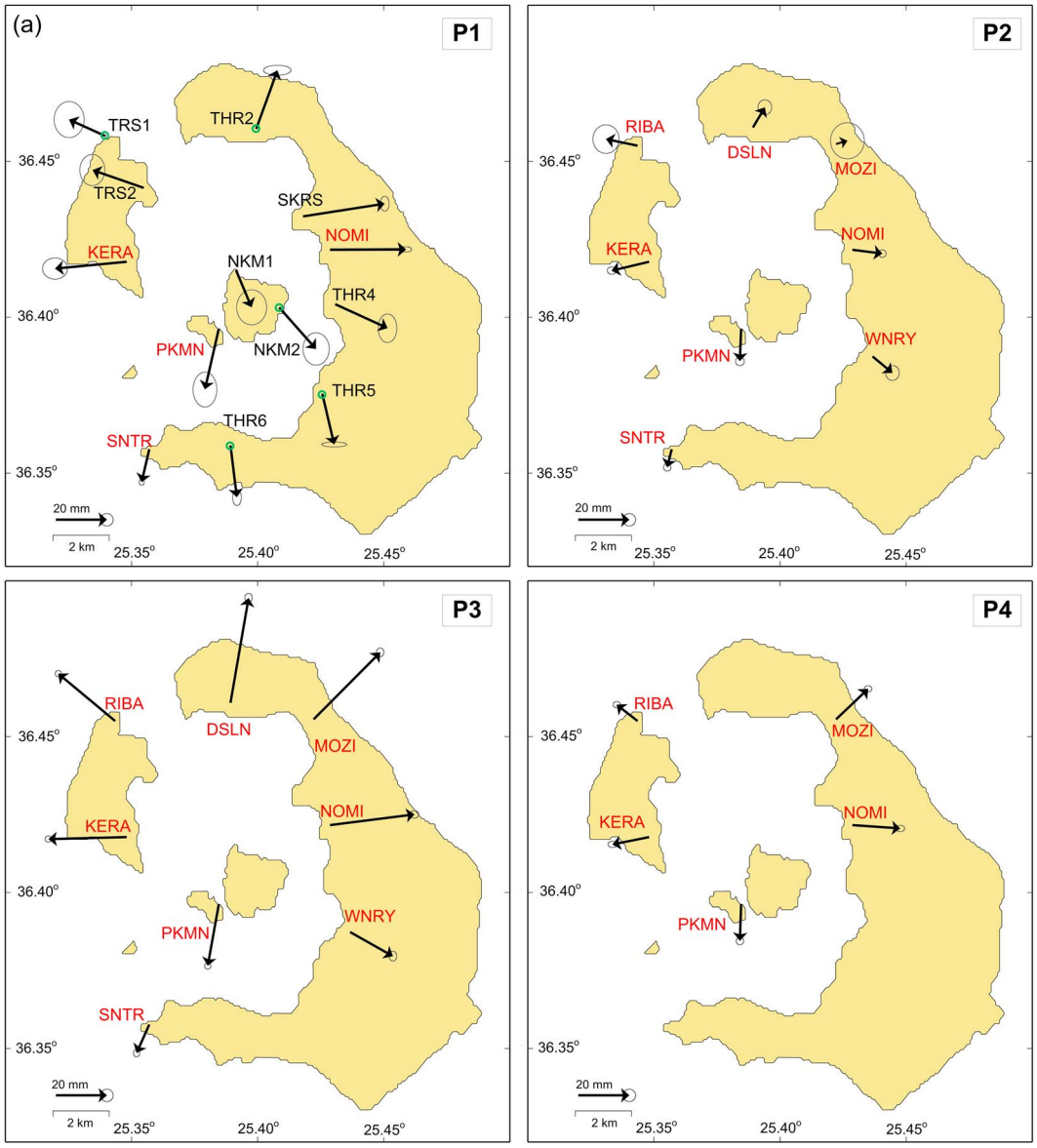

Figure 6. Displacement vectors used in this study for each period of deformation. Permanent stations are indicated with red characters and survey stations with black; 1σ error ellipses and intervals are shown. Nearly radial displacements characterize the whole period, but displacements during P1 and P3 are 2 times larger than in P2 and P4, while those of P5 are insignificant. (a) Horizontal displacements for P1 to P4. In P1 open green circles indicate GPS stations used in the sensitivity analysis. (b) Vertical displacements for P1 to P4. (c) Horizontal and vertical displacements for P5. Mark that the displacement scale has been doubled.

and are summarized in Figures 1 and 5. Figure 5a in particular provides evidence of two major seismicity periods, January–June 2011 and October 2011 to January 2012.

Fluctuations in seismicity were compared with the GPS displacements, for a wider period than that examined in *Newman et al.* [2012]. For simplicity and because the records of station NOMI (see section 5) was the most complete and there exists a strong correlation between vertical and horizontal displacements in Figure 6, mean monthly vertical deformation of NOMI was regarded as representative of the overall deformation and was plotted in Figure 5b.

The concurrent behavior of seismicity and mean displacement rates permits the identification of five periods (P1–P5), each 3 to 6 months long, summarized in Table 1. The length of these periods is compatible with the

©2014. American Geophysical Union. All Rights Reserved.

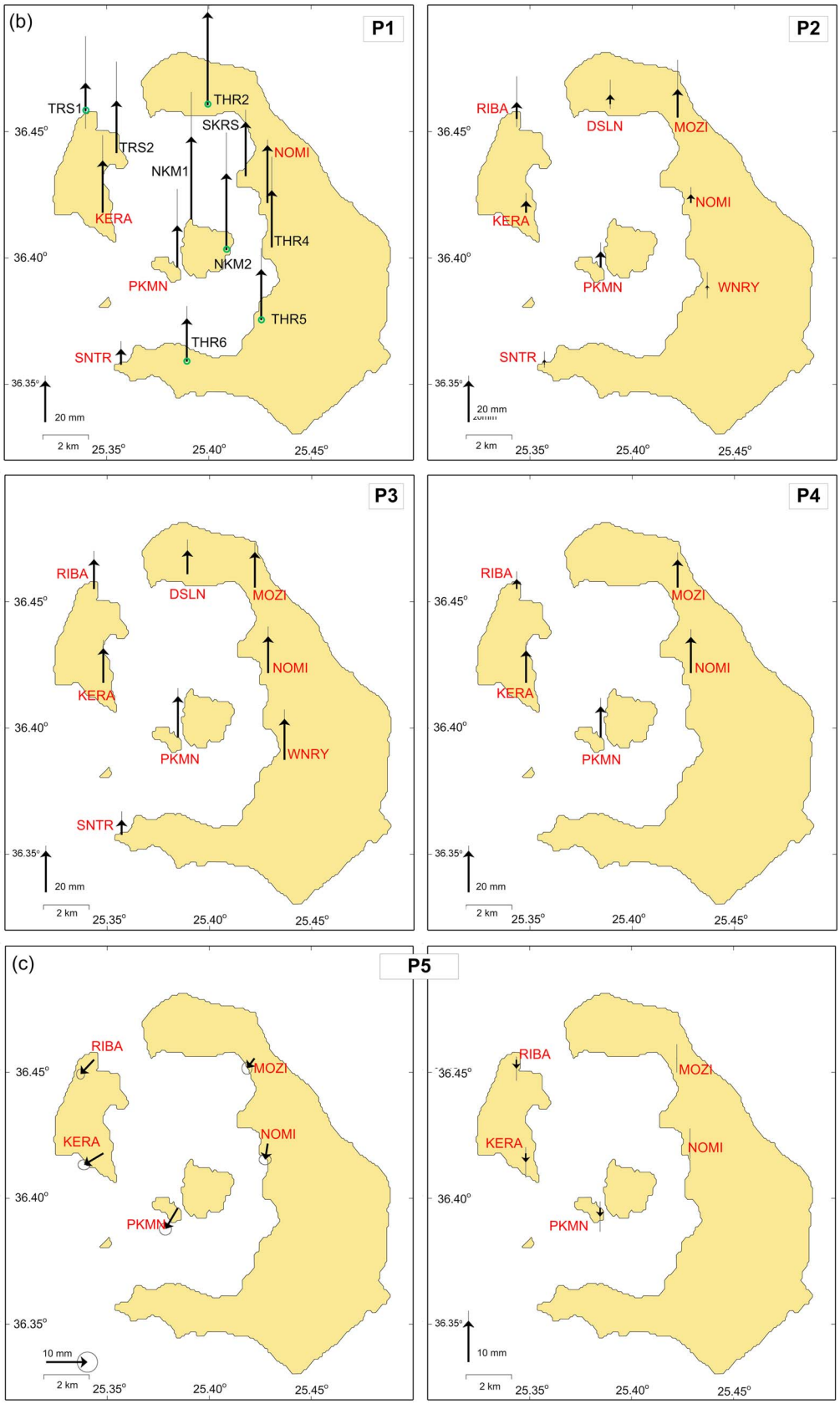

Figure 6. (continued)

©2014. American Geophysical Union. All Rights Reserved.

Table 1. Monthly Mean Seismicity ($M_L \geq 1.0$) and Representative Displacement Rates Permitting to Document Five Deformation-Seismicity Periods

Period	Date	Duration (Months)	Mean Earthquake Frequency (Events/Month)	Displacement (mm/Month)
P1	Jan–Jun 2011	6	64	6.1
P2	Jul–Sep 2011	3	27	2.4
P3	Oct 2011 to Jan 2012	4	126	7.5
P4	Feb–May 2012	4	17	5.7
P5	Jun–Sep 2012	3	3	−1.0

typical length of deformation phases in other volcanoes [*Galgana et al.*, 2014] and is corroborated by the analysis of micro-earthquakes by *Konstantinou et al.* [2013]. Still, our division in five periods is finer due to its basis on ground displacements. The adopted division was also corroborated by the fact that micro-earthquakes with magnitude >3 were confined to P1 and P3.

After P5, the intracaldera seismicity and continued deformation were nearly null, with the exception of a small swarm in May 2013 (about 10 micro-earthquakes at the NE edge of the KL), possibly correlating with a transient vertical displacement of the order of 5 mm noticed in several GPS stations (http://geophysics.eas.gatech.edu/anewman/research/Santorini/; http://geophysics.geo.auth.gr/ss/; www.gein.noa.gr). This indicates that no significant deflation succeeded the 2011–2012 caldera inflation period.

5. GPS Data

GPS data analyzed primarily come from permanent stations, mostly operated by the Georgia Tech and Patras University, and are freely accessed through the University NAVSTAR Consortium, Boulder, Colorado (UNAVCO) webpage. Data used are summarized in Figure 6.

During the wider monitoring period two moderate earthquake swarms occurred in the vicinity of Santorini and produced relatively high accelerations and much concern among the population, the 26/06/2009 $M_L = 5.0$ earthquake [*Krizova et al.*, 2010] and the 27.01.2012 $M_W = 5.3$ earthquake [*Kiratzi*, 2013]. Both events left no significant trace on the GPS records and seem not to be related to intracaldera effects. Hence, all observed deformation seems to be related to local magmatic effects.

Our analysis is based on daily solutions using GPS Inferred Positioning System-OASIS software supplemented with survey solutions. From daily solutions, mean displacements and their mean misfits (uncertainties), which broadly correspond to white noise were computed. Using a semiempirical formula derived from GPS stations in Greece (equation (6.11) in *Hollenstein* [2006]), the total noise, a combination of white and time-dependent noise, was computed (Figure 6). These values of noise are consistent with more recent estimates of total noise in GPS data in northern Greece [*Mouslopoulou et al.*, 2014].

Approximate, flat values of 3 mm for horizontal and 5 mm for vertical displacements, covering both permanent and survey stations were then adopted (1σ) in equation (3). It is evident that displacements observed are statistically significant for periods P1 through P4 but not for P5.

6. Data Analysis

Our analysis was made for each of the five periods and by assuming both a single and a double source.

6.1. Data Sets Analyzed per Deformation Interval

In our study we used all the available GPS for each of the five periods, P1 to P5.

P1. Data from four permanent GPS stations (NOMI, KERA, PKMN, and SNTR) and in addition data from nine stations from the 2010 and 2011 surveys (Figure 6), based on the assumption that no ground deformation occurred before January 2011, as is corroborated by permanent GPS stations [see *Newman et al.*, 2012]. In addition, for a sensitivity analysis, we repeated the modeling using five of the nine survey stations.

P2–P3. Data from the existing/available eight permanent GPS stations.

P4–P5. Data from the existing/available five permanent GPS stations.

©2014. American Geophysical Union. All Rights Reserved.

Table 2. Details of the Parameters of the Grid G Initially Used in the Modeling[a]

			Spacing	
	Min	Max	One Source	Two Sources *(Preliminary Grid)*
φ (°)	36.3790	36.4613	0.0018	0.0090
λ (°)	25.3334	25.4208	0.0022	0.0111
d (km)	0.5	10.0	0.2	1.0
ΔV (10^6 m^3)	1.0	10.0	0.2	0.5
	−6.0*	6.0*		
Number of grid points			~4.2×10^6	~290×10^6

[a]Smaller grids with finer analysis were adopted after the first search. An asterisk marks the parameters used in P5.

6.2. Grid Selection

As noted in section 3, a requirement of the TOPINV algorithm is to a priori define an R^n grid of possible solutions of the system of equations (grid G). In the grid adopted, magma sources can practically correspond to any point of the caldera (Figure 1), while the source depth can range between 0.5 and 10 km and the volume change between 1 and 10×10^6 m^3. For P5, in order to account also for possible deflation affects, a range of $\Delta V = -6 \times 10^6$ to 6×10^6 m^3 was assumed. The details of this grid are shown in Table 2.

The above a priori conditions used to construct grid G do not exclude any possible solution and do not introduce any bias; hence, they can be assumed to lead to "objective" solutions.

As noted above and analyzed in *Saltogianni and Stiros* [2013b], we conclude to a "nested grid" solution by making the inversion in steps for all variables by using a gradually smaller and finer grid. This was necessary in the case of modeling a double source, where the unknown variables are 8 and the number of grid points tends to become very large.

6.3. Weighting of Observations

Observations of horizontal and vertical displacement were weighted according to their standard deviations, 3 mm and 5 mm, respectively, and these values were introduced in equation (3).

7. Results

7.1. Single Spherical Source

The results of our modeling for the four first periods P1 to P4 are summarized in Table 3 and in Figure 7. The latter shows the location of the modeled source, as well as the observed and predicted GPS displacements. Standard errors of each variable are small while the quasi-independently computed misfit between modeled and measured displacements is excellent (mean misfit 0.2–0.7 cm).

Table 3. Best Estimates and 1σ Uncertainties (Italic Font) of the Variables of the Modeled Single Mogi Sources (See Figure 7) for Each Period[a]

	P1		P2	P3	P4
	M1	(M1)	M1	M1	M1
Latitude (°)	36.431	(36.432)	36.433	36.426	36.428
	±0.02	*(±0.02)*	*±0.02*	*±0.02*	*±0.01*
Longitude (°)	25.385	(25.393)	25.388	25.390	25.390
	±0.02	*(±0.02)*	*±0.02*	*±0.01*	*±0.01*
Depth (km)	4.8	(5.4)	3.2	2.8	3.4
	±0.22	*(±0.20)*	*±0.19*	*±0.10*	*±0.20*
ΔV (10^6 m^3)	6.1	(7.5)	1.5	3.6	2.4
	±0.46	*(±0.43)*	*±0.14*	*±0.10*	*±0.18*
Mean misfit (cm)	0.65	0.58	0.35	0.67	0.19
χ^2_v	2.87	2.75	1.16	4.29	0.40

[a]In parentheses, the results of a sensitivity analysis using a smaller number of observations (see section 7.5).

©2014. American Geophysical Union. All Rights Reserved.

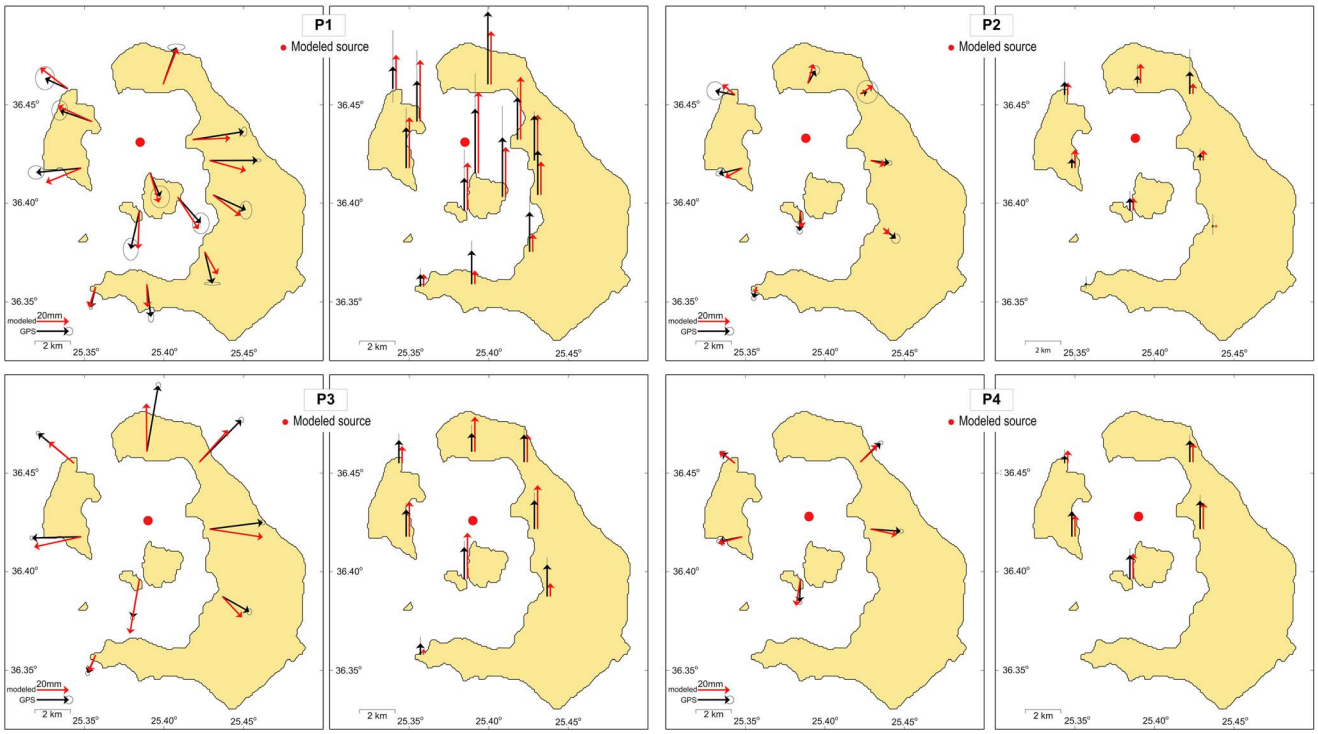

Figure 7. Modeling of a single spherical magma source. Observed displacements (black vectors), modeled sources (red circles), and the corresponding modeled horizontal and vertical displacements (red vectors) for P1 to P4.

Our data revealed some persistence in the location of the source during P1 to P4, close to the location defined by previous studies (see section 1); however, the depth/volume plot of Figure 9 may reveal a source becoming shallower and smaller since P2.

7.2. Double Source Modeling

The results of our modeling for the first four periods are summarized in Table 4 and in Figure 8. Their precision is very good as can be derived from standard and mean misfit errors and better than for the single source modeling (see Tables 3 and 4). At a first view, our results indicate some persistence in the location of a first source M1 at the north part of the caldera, but smaller and shallower than what was previously determined, and also a second, deeper source M2, with variable characteristics (Figure 9). For P2, M2 is located in the northern part of the caldera, while during P1, P3, and P4, it correlates with the KL.

Table 4. Estimation and 1σ Uncertainties (Italic Font) of the Variables of the Modeled Double Mogi Sources (See Figure 8) for Each Period[a]

	P1				P2		P3		P4	
	M1	M2	(M1)	(M2)	M1	M2	M1	M2	M1	M2
Latitude (°)	36.440	36.401	(36.437)	(36.405)	36.429	36.444	36.432	36.398	36.429	36.392
	±0.02	*±0.03*	*(±0.02)*	*(±0.03)*	*±0.03*	*±0.03*	*±0.01*	*±0.02*	*±0.01*	*±0.05*
Longitude (°)	25.387	25.388	(25.392)	(25.399)	25.378	25.410	25.388	25.383	25.393	25.369
	±0.01	*±0.04*	*(±0.01)*	*(±0.04)*	*±0.01*	*±0.05*	*±0.01*	*±0.01*	*±0.01*	*±0.07*
Depth (km)	3.3	6.4	(3.3)	(7.3)	1.5	7.2	0.6	8.0	2.5	7.6
	±0.20	*±0.32*	*(±0.12)*	*(±0.24)*	*±0.00*	*±0.87*	*±0.10*	*±0.27*	*±0.14*	*±0.76*
ΔV (10^6 m^3)	2.7	3.5	(2.9)	(4.0)	0.75	1.6	1.8	5.7	1.5	2.0
	±0.24	*±0.33*	*(±0.12)*	*(±0.26)*	*±0.01*	*±0.29*	*±0.08*	*±0.27*	*±0.07*	*±0.39*
Mean misfit (cm)	0.56		0.51		0.31		0.39		0.15	
χ^2_v	2.81		2.88		1.46		1.83		0.33	

[a]In parentheses, the results of a sensitivity analysis (see section 7.5).

©2014. American Geophysical Union. All Rights Reserved.

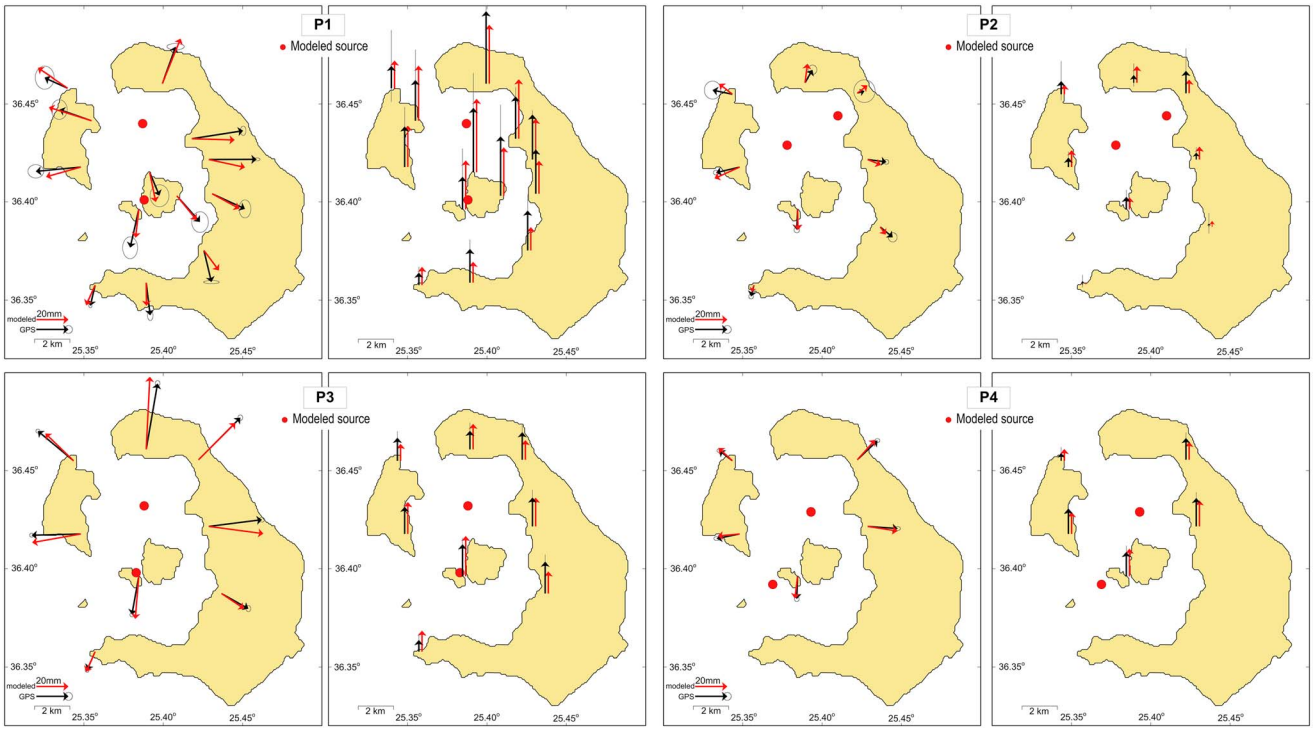

Figure 8. The same as Figure 7 but for the modeling of two Mogi sources (M1 and M2).

7.3. The Problem of Period 5

While modeling for both one and two sources was successful for periods 1 to 4, no reliable source models were obtained for P5. This indicates that the underlying magmatic process cannot be explained by expansion and/or contraction of one or of two-point spherical sources, and the algorithm adopted can identify cases not leading to a solution and hence tends to avoid "false alarms" [cf. *Saltogianni and Stiros*, 2013b].

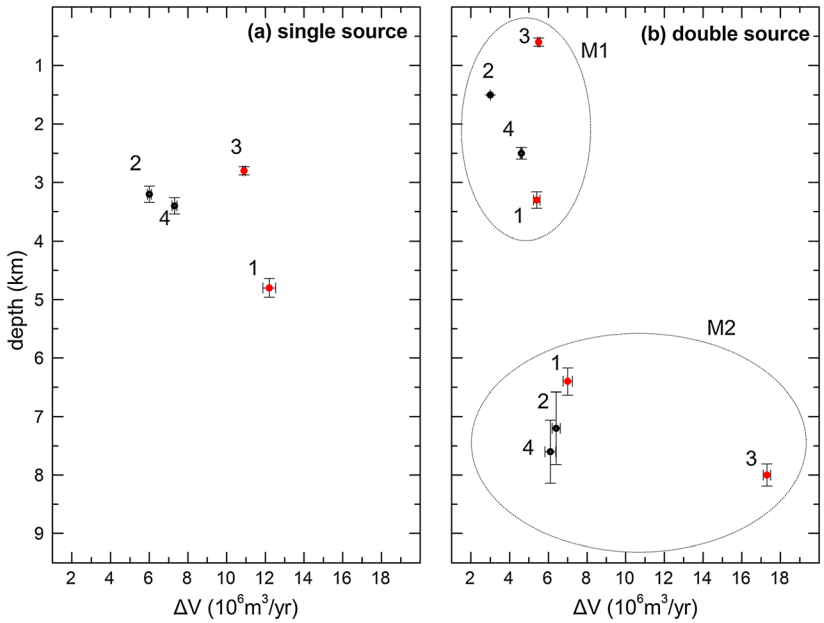

Figure 9. Plot of the estimates of depth (km) and volumetric change ΔV for (a) the single and (b) the double-modeled sources for each of the four examined periods, marked by numbers 1 to 4. Error bars indicate 1σ uncertainties. Sources corresponding to high deformation/seismicity intervals are shown in red.

©2014. American Geophysical Union. All Rights Reserved.

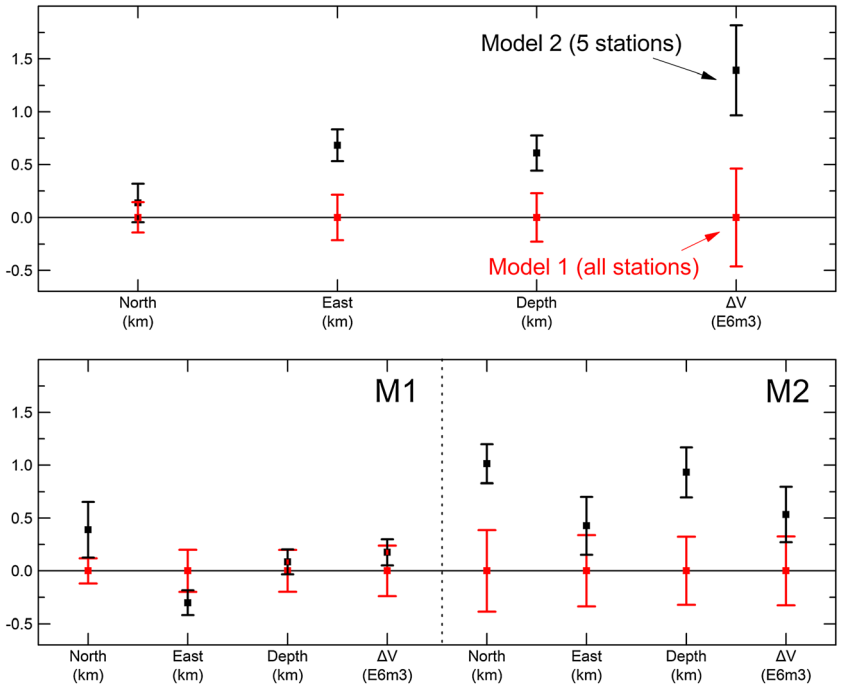

Figure 10. Results of the sensitivity analysis for P1. "Model 1" indicates the solution with all stations in Figure 6, "Model 2" using only five stations (see Figure 6); 1σ uncertainties are shown. The estimates of the four variables defining magma sources are statistically similar at the 95% confidence level.

A possibility is that P5 reflects partial viscoelastic relaxation, a problem that is beyond the scope of this work, or that displacements during this period were too small, equal to, or even below the level of uncertainty of geodetic measurements to permit a safe modeling.

7.4. Limitations in the Mogi Modeling

Modeled spherical sources are small (Tables 3 and 4) and satisfy the conditions for application of the Mogi model [*Mogi*, 1958; *McTigue*, 1987]; in addition, their separation is large enough (several kilometers) for sources with a radius mostly smaller than 100 m (Figure 12) to satisfy the requirements for elasticity due to their interaction [*Pascal et al.*, 2013].

Furthermore, the topography in Santorini is essentially smooth and does not a priori exclude elastic modeling [*Cayol and Cornet*, 1998; *Williams and Wadge*, 1998; *Lundgren et al.*, 2003; *Masterlark*, 2007], an effect already confirmed by the use of synthetic data [*Saltogianni and Stiros*, 2013b].

7.5. Significance and Stability of Results

Modeling of the deformation during the five periods was not based on entirely uniform data, with P1 characterized by fewer permanent stations but more stations in total than in the subsequent periods (Figure 6). For this reason, in order to exclude the possibility the obtained results to reflect only differences in data used, a sensitivity analysis was made for P1 by using a smaller database (five survey stations). Results, however, were essentially similar (Tables 3 and 4 and Figure 10), indicating a stability of the solution for the specific period and compatible/uniform quality results for all the periods.

8. Modeled Intrusions and Seismicity

Modeling of periods 1 to 4 by a single Mogi source permitted statistically significant solutions (Table 3) and indicates a somewhat stable pattern (Figures 7 and 9) that cannot provide any explanation for seismicity along KL (Figure 3) or for the observed fluctuations in the seismicity rates (Figure 5). On the contrary, modeling each period with two sources revealed an intrusion pattern changing in space and in time (Figures 8 and 9) that, as will be shown below, can well explain seismicity.

©2014. American Geophysical Union. All Rights Reserved.

Table 5. Estimates and Uncertainties (Italic Font) of the Parameters of the Mogi Sources for the Aseismic Inflation Period of 1994–1999

	June–November 1994	November 1994 to June 1995	March 1996 to June 1999
Latitude (°)	36.419	36.430	36.440
	±0.002	*±0.000*	*±0.003*
Longitude (°)	25.358	25.369	25.392
	±0.002	*±0.002*	*±0.004*
Depth (km)	0.50	1.30	1.90
	±0.07	*±0.40*	*±0.80*
ΔV (10^6 m^3)	0.10	0.30	0.72
	±0.01	*±0.03*	*±0.14*

Sources at the north part of the caldera seem much smaller (Figure 8) at such a distance from the seismicity of the KL. During P2, two sources were obtained at the north part of the caldera, and this probably indicates either the presence of two different sources, one shallow (1500 m) and one deep (7300 m), or perhaps source complexities which cannot be fully resolved by the adopted Mogi model. Interestingly, these sources correlate with the CL and with the modeled magma sources of the aseismic inflation period of 1994–1999 [*Stiros et al*., 2010] if the latter is assumed to be composed by three distinct events (Table 5 and Figure 11) and not as single event as proposed by *Saltogianni and Stiros* [2012a].

8.1. Correlations Between Magma Sources and Seismicity

Summarizing results in Figure 12 (assuming for simplicity only one source during P2), it seems that sources M1 along CL produced no micro-earthquakes (as was also the case of the aseismic inflation interval of 1994–1999; see above), and sources M2 correlating with KL produced seismicity during P1 and P3. This may indicate a genetic relationship between magma sources and seismicity, schematically summarized in Figures 13a and 13b. The apparent problem is source M2 during P4. The explanation is that source M2 in P4 is smaller than in P1 and P3 (Table 4) and during P4 is located at the extension of the KL, and as equation (1) predicts, the stresses by this smaller source at a longer distance are too small to generate seismicity. This situation is schematically explained in Figure 13c.

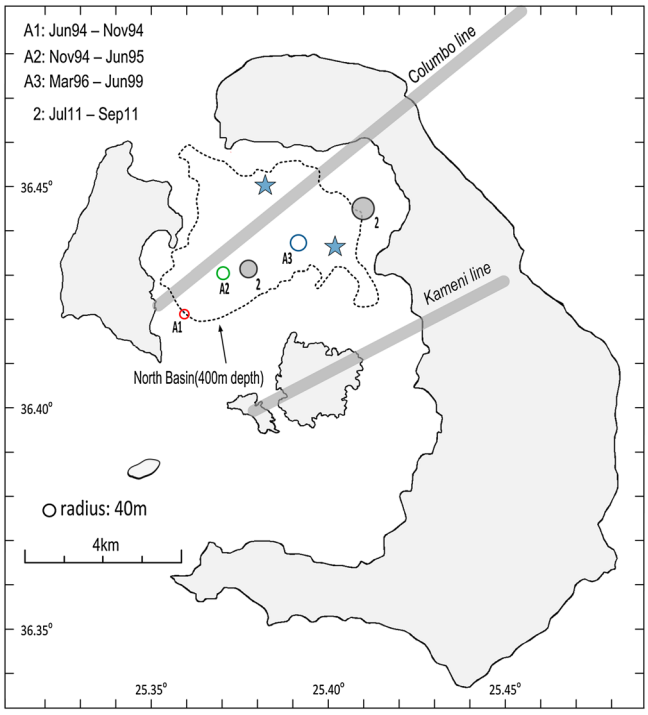

Figure 11. Mogi sources for the aseismic inflation period of 1994–1999 (open circles marked A1, A2, and A3), based on the data of Table 5. The 2011–2012 sources during P2 are also shown with filled circles along with symbol "2". Mark the correlation of these sources with the CL. Stars indicate major shallow intrusions derived from marine surveys (see Figure 15).

8.2. Coulomb Failure Stress Modeling

This qualitative explanation for the generation of seismicity was tested through the calculation of Coulomb failure stresses (CFSs) changes. Using the modeled source locations and volume changes (Tables 3 and 4), CFSs were computed for the four periods in which we were able to determine spherical pressure sources. CFSs were computed both for individually and dual sources using the COULOMB 3.3 software [*Toda et al*., 2005]. The models all estimate the CFSs of a right-lateral receiver fault striking N74°E and dipping 88°N, with coefficient of friction of 0.4, a standard value for continental faulting as suggested by *Toda et al*. [2005].

©2014. American Geophysical Union. All Rights Reserved.

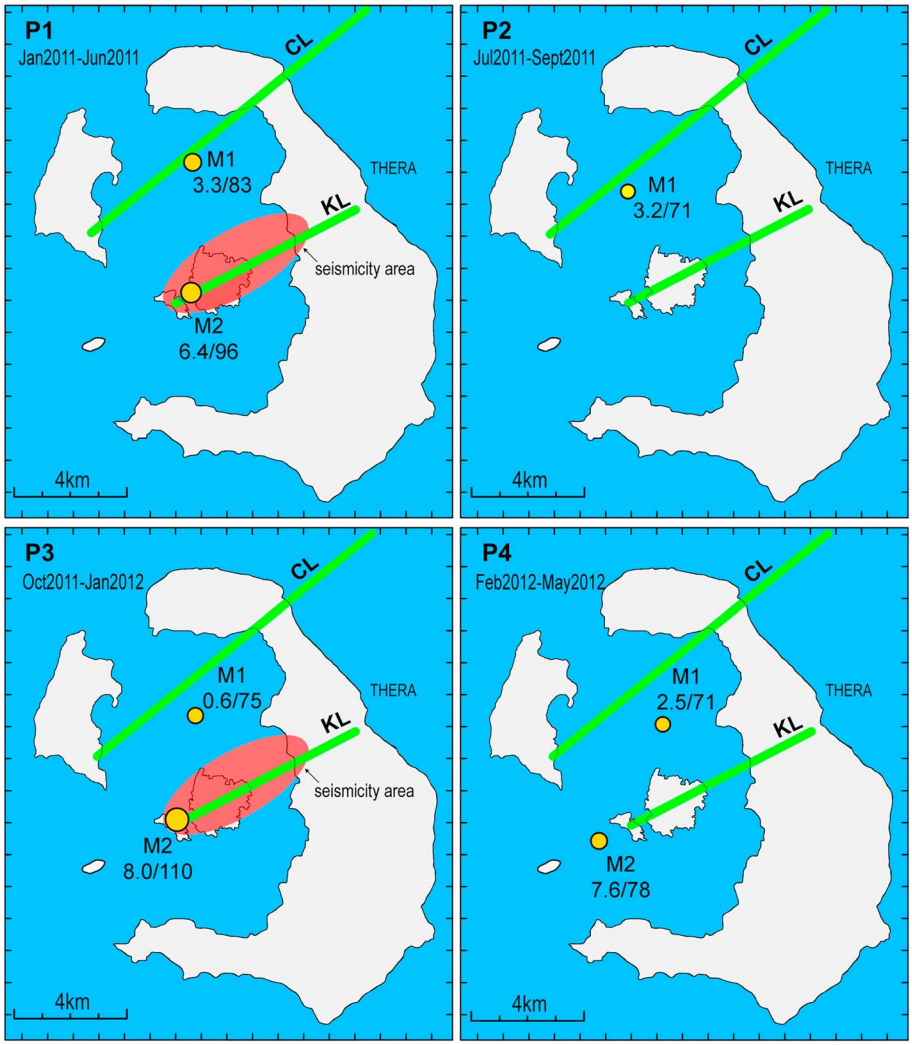

Figure 12. Summary and conceptual model for the relationship between intrusions (spherical sources, M1, M2) and seismicity (red ellipses) during the unrest period of January 2011 to May 2012 and the four critical subperiods. Earthquakes are confined to periods P1 and P2 and are correlating with intrusions along the KL, most probably the first time since the last eruptions of 1950. Magma intrusions along or close to the CL, on the contrary, are more frequent and reach to shallow levels and dominate the surface deformation pattern but are arrested by plastically deforming strata and are not associated with seismicity. Next to each source (green circles), numbers indicate depth (kilometers, numerator) and the corresponding radius of the intrusion (meters, denominator). P2 is shown with one single source for simplicity.

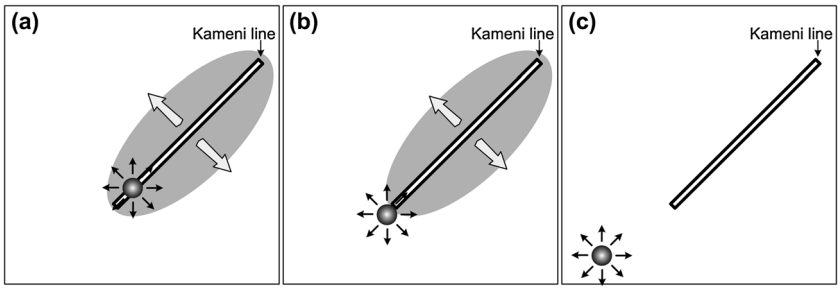

Figure 13. Schematic explanation for the contrast in seismicity in periods P1, P3, and P4 (plan view). (a, b) In P1 and P3 the magma source is inside or too close to the KL, and the level of deviatoric stresses (equation (1)) is high enough to produce rupture and earthquakes. (c) Stresses are highly attenuated, and stresses generated at KL are below the threshold of fracturing; this explains the absence of seismicity during P4.

©2014. American Geophysical Union. All Rights Reserved.

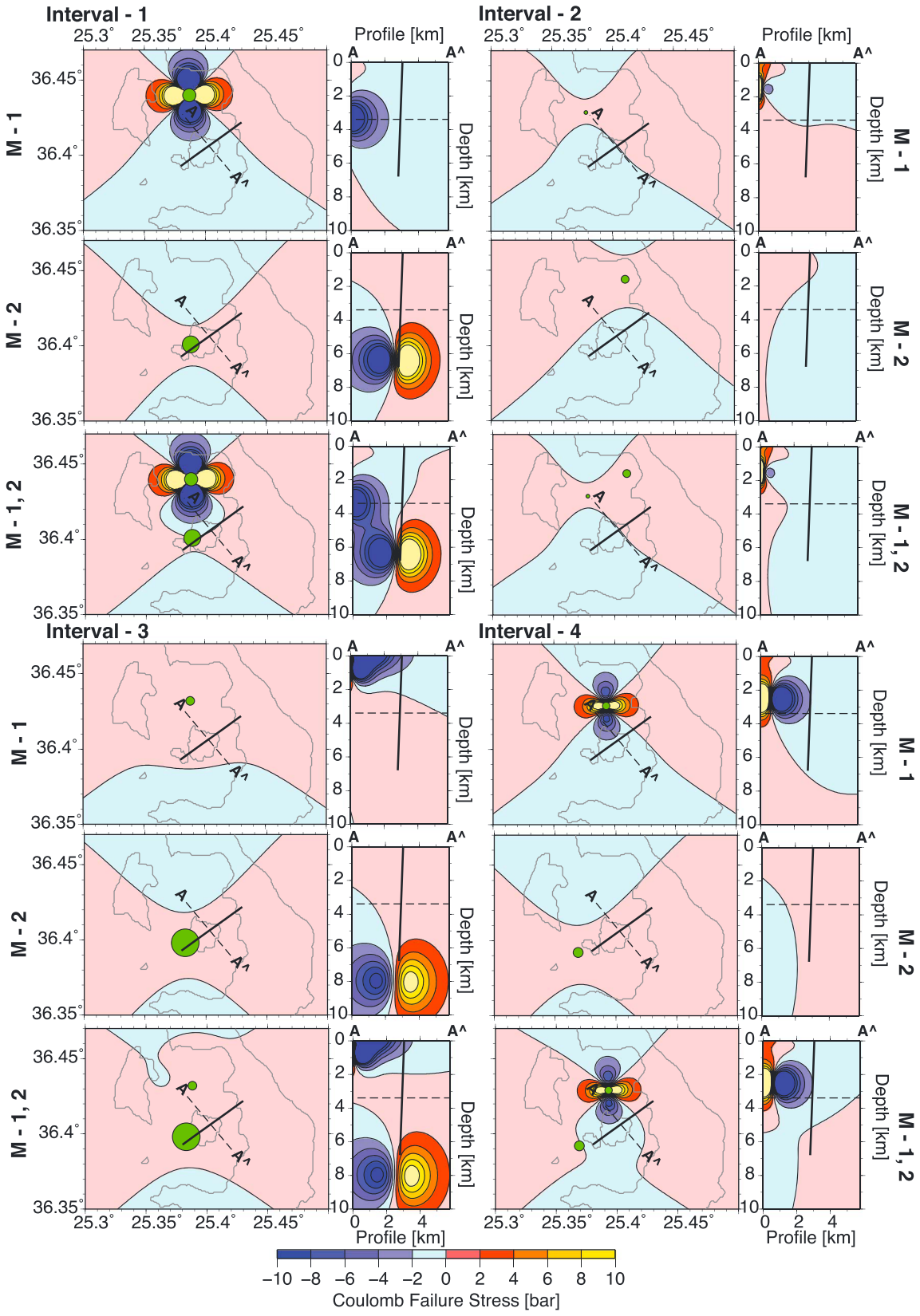

Figure 14

©2014. American Geophysical Union. All Rights Reserved.

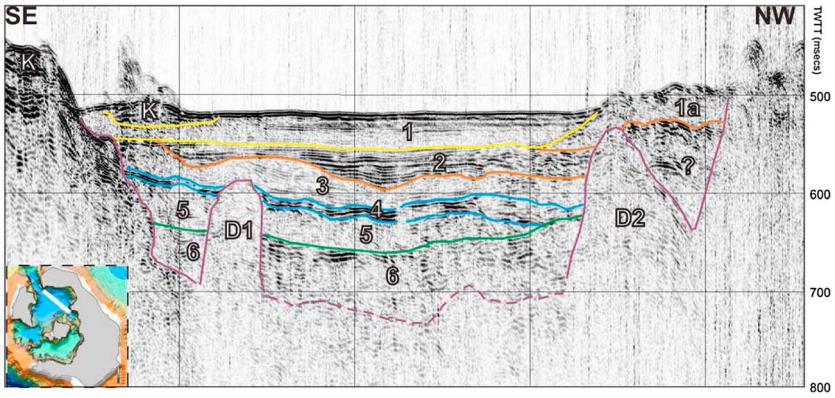

Figure 15. Seismic stratigraphy at the north part of the Santorini basin, based on an air gun 10ci single channel seismic profile. Location map in the inset. D1 and D2 indicate intrusions, and layer 1 is post-Minoan; 100 msec correspond to approximately 120 m [after *Sakellariou et al*., 2012]. D1 and D2 are marked in Figure 11.

The receiver fault, which represents the KL, was determined as a single plane that best describes the intracaldera seismicity using singular value decomposition (SVD). Figure 14 shows the results of these models in plan view and cross section near the midpoint of seismicity (3.4 km depth) along the SVD determination of the KL.

In agreement with qualitative estimations, CFSs produced by any source in the vicinity of the CL (M1 sources) is not at a level to produce shear rupture along the KL. This is also the case with the M2 source at the extension of the KL during P4, and this explains the drop of seismicity during this period.

Source M2 correlates well with the KL for P1 and P3 and seems to explain the two swarms of seismicity in terms of direct or of lateral spreading, as is schematically shown in Figures 12 and 13. In contrast, source M2 in P2 and P4 cannot generate the necessary stresses (CFSs) and seismicity along KL (Figure 14).

8.3. Shallow and Aseismic Intrusions

Our modeling of two magma sources for P2 and P3 revealed very shallow sources at the northern basin of the Santorini caldera, 1.5 and 0.6 km, respectively, corresponding to rather small-scale intrusions (0.8 and 1.8×10^6 m^3, respectively), slightly stronger than those inferred for the 1994–1999 period (Table 5). Such very shallow intrusions may appear questionable, i.e., artifacts of modeling.

However, the sensitivity analysis of *Saltogianni and Stiros* [2013b] indicates that the inversion algorithm and the pattern of data used can identify such shallow sources, while marine geophysical surveys in the critical area provide evidence of shallow major, eventually post-Minoan intrusions (Figure 15) [*Sakellariou et al*., 2012].

We therefore conclude that at the northern part of the caldera, uppermost crustal layers are likely to deform plastically and to have enough strength to arrest even very shallow (0.5–4 km) intrusions [cf. *Gudmundsson*, 2006] without seismicity, even if stress changes predicted by CFSs are sufficient along CL (Figure 14). Interestingly, a low-velocity area for seismic waves has been identified in the wider area [*Dimitriadis et al*., 2010].

On the contrary, intrusions along the KL, the area for which all post-Minoan eruptions have been confined [*Pyle*, 1990; *Pyle and Elliott*, 2006; *Druitt et al*., 2012], are deeper (6.5–8 km) and tend to be associated with seismicity. These intrusions may also testify to a different feeding system [*Fabbro et al*., 2013] and perhaps different magma characteristics.

Figure 14. Coulomb failure stresses (CFSs) for the periods 1–4 corresponding to each of the two sources modeled (sources M1 along CL and M2 along KL) and to their combination using a uniform color scale. Only M2 sources in P1 and P3 can produce stresses at a level necessary to generate microseismicity along KL. In each interval, CFSs are shown in plan view near the mid-depth of microseismicity (3.4 km) and to the right in profile (marked by the dashed line AA′ in plan view). The SVD-determined KL is shown by the dark solid line in both plan view and profile images (see section 8.2).

©2014. American Geophysical Union. All Rights Reserved.

Table 6. Parameters and Uncertainties (Italic Font) of Modeled Sill and Dyke During P3 (See Figure 16)[a]

	Sill		Dyke	
Depth (km)	2.5	*±0.28*	1.3	*±0.30*
Strike (°)	5.0	*±4.10*	84.0	*±4.00*
Length (km)	3.8	*±0.50*	4.0	*±0.25*
Width (km)	3.0	*±0.25*	2.5	*±0.25*
Opening (cm)	60.0	*±30*	30.0	*±10*
Mean misfit (cm)	0.73 (0.39)			
χ^2_v	10.70 (1.83)			
ΔV (10^6 m^3)	6.90 (1.80)		3.00 (5.70)	
Total ΔV (10^6 m^3)	9.90 (7.50)			

[a]In parentheses, the corresponding values for double Mogi sources.

9. Alternative Models

An a priori assumption of this study is that the deformation was due to magmatic effects, and hence, hydrothermal or better hybrid effects [*Gottsmann et al*., 2006] were ignored. The reasons for that are (i) the difficulties and uncertainties in modeling deformation produced by hydrothermal fluids [*Fournier and Chardot*, 2012], (ii) the observed short-term fluctuations in seismicity and deformation rates (Table 1) which are consistent with the hypothesis of pulses of magma discussed below, (iii) the absence of significant surface deformation for 2 years after the unrest, and (iv) during the critical period there were no reports for significant changes in the outflow of surface hydrothermal vents, which are abundant in various parts of the caldera [*Sigurdsson et al*., 2006]. Of course, these arguments cannot exclude the hypothesis of hybrid (magmatic/hydrothermal) effects, mainly because geodetic data alone do not constrain the source material responsible for pressure change. Still, wherever the origin of deformation is in the north part of the caldera, stresses generated there cannot explain the clusters of microseismicity along the KL (Figure 14).

The overall analysis is based on the assumption of an elastic, homogeneous medium as required by the analytic Mogi model. In order to assess results presented, we investigated whether analysis of the same data using an alternative modeling scenario may lead to results supporting the double Mogi modeling. In particular, the possibility of describing the caldera deformation of each period in terms of sills and dykes was investigated using the conditions and equations of *Okada* [1985]. In this case a rectangular opening filled by magma is defined by eight variables (parameters), easting and northing of the center of the rectangles, depth of the upper tip, strike and dip, length and width of the rectangular and the amount of opening [*Okada*, 1985].

In agreement with the results of *Newman et al*. [2012] for a shorter time interval, it was found that no successful sill or dyke modeling can be obtained for each of the five periods examined here. For this reason, we tested modeling of a combination of a rectangular vertical dyke (dip = 90°) and of a rectangular horizontal sill (dip = 0°), of uniform opening, separately for each period. Results are reported here for P3, the most energetic one, and representative of all periods and of the significance of this modeling.

The Okada equations for the two concurrent sources lead to a system of 14 unknowns with 24 observations for P3. The TOPINV algorithm was used for a grid covering all possible reasonable values of the variables in order to obtain an objective, as possible, solution with the following assumptions: the location of the sill was allowed to be anywhere at the north part of the caldera (cf. Figure S4 in *Newman et al*. [2012]) while the location of the dyke in the vicinity of the Kameni islets and the KL; for both the sill and dyke, all possible orientations were allowed, while the depth of their upper tip was allowed to be in the range of 0–6 km and their dimensions between 1 and 7 km. The only subjective constraint was the opening of the dyke or sill, allowed to be between 0 and 1.0 m, the approximate limits commonly observed in various volcanoes [e.g., *Annen et al*., 2001].

Optimal model solutions are summarized in Table 6 and Figure 16. The misfit between observations and predicted displacements is good (0.73 cm; see Table 6 and Figures 16b and 16c), but estimations of most variables are noisy (Table 6), while the strike of the dyke deviates from that of the KL and the direction of earthquake epicenters and the volume of intrusions is much larger than in the spherical models. Still, the main output of this modeling is that it tends to associate the deformation with two distinct magma sources, a dyke correlating with the KL and a sill farther north. If alternatively a dyke with a larger opening is allowed (opening up to 10 m [see *Annen et al*., 2001]), the algorithm identifies a *second*, independent

©2014. American Geophysical Union. All Rights Reserved.

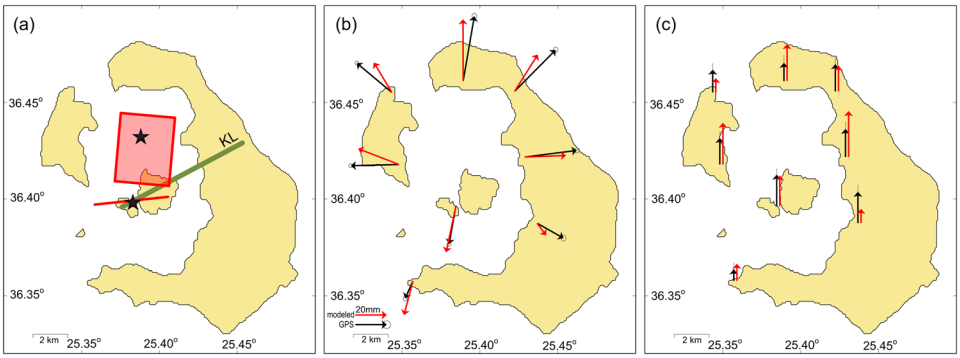

Figure 16. (a) Modeling of the deformation during the most energetic period P3 as a combination of a horizontal sill (rectangle) and of a vertical dyke (red line). KL and the location of the two Mogi sources (black stars) in the corresponding period are shown in map view. (b and c) Observed and predicted horizontal and vertical displacements.

solution (i.e., another pair of a dyke and of a sill) with a dyke with much smaller dimensions (less than 1 km) but with an opening of approximately 9.5 m. This second solution can be discarded.

10. Discussion

In the past, Mogi models were usually based on a rather small number of 1-D data (leveling, tilting etc. [*Gottsmann et al.*, 2006; *Poland et al.*, 2006]) and standard inversion algorithms. In the case of Santorini it was possible to use high-quality 3-D data leading to redundant systems of observation equations and a new topological algorithm that may identify with precision several alternative solutions. In addition, the computed double Mogi sources for each period can explain the pattern and fluctuations of seismicity and are broadly consistent with the modeling based on a very different model (Okada equations, Figure 16).

The simple model (Mogi model) defined by few variables (four variables for each magma source), by relatively high redundancy, and by "objective" initial conditions (a reasonable possible range of each variable) led to more precise, stable results (Table 4 and sensitivity analysis) with more clear physical significance than the more elaborate Okada model which requires more variables (up to eight variables) but inevitably requires some somewhat subjective initial conditions (a priori range estimates of certain variables) and is characterized by smaller redundancy. In addition, the double Mogi model is much more precise than the Okada Model (e.g., for P3 mean misfits 0.39 and 0.73 cm, respectively, and χ^2_v; 1.83 and 10.7, respectively; see Table 6). This may indicate that adaptation of a more realistic model to describe the deformation of Santorini (i.e., of a model not based on the simplified hypothesis of an elastic and homogenous medium) without additional information may not lead to differences in modeled intrusion models beyond the uncertainty of the observations and of background model assumptions. This may explain also why all investigators of the recent unrest of Santorini on the basis of deformation data were practically confined to Mogi sources [*Newman et al.*, 2012; *Parks et al.*, 2012; *Foumelis et al.*, 2013; *Lagios et al.*, 2013; *Papoutsis et al.*, 2013]. Of course, the efficiency of the Mogi models may be due to the analysis of short duration periods corresponding to small volumes of intrusions, producing effects perhaps better modeled by simple models, even if effects such as pressure changes cannot be modeled independently using geodetic data only.

The modeling of deformation during short distinct periods of the unrest of 2011–2012 (Figure 5) [cf. *Konstantinou et al.*, 2013; *Galgana et al.*, 2014] and on the basis of two different sources permitted the observation of an unstable and complex pattern of intrusions with a selective relationship with the intracaldera seismicity.

Magma sources at the northern part of the caldera, correlating with CL, seem aseismic (Figure 12), in agreement with the results of modeling a previous longer episode of caldera inflation [*Stiros et al.*, 2010; *Saltogianni and Stiros*, 2012a] (Table 5 and Figure 11), but they overshadow the effects of other, deeper and stronger sources along or close to the KL (sources M2). If the stresses generated by these last sources surpass a certain threshold, depending on their distance from KL and their volume (see equation (1)), seismicity is generated, as was observed during P1 and P3 and is predicted by CFSs (Figure 14).

©2014. American Geophysical Union. All Rights Reserved.

If the above model is correct, it indicates that the near-surface rocks around the CL may arrest rather frequent intrusions either due to increased strength or substantial changes in the layered stress regime [*Gudmundsson et al*., 1999; *Gudmundsson*, 2006]. This is probably the reason why the post-Minoan history of Santorini is associated only with eruptions along the KL [*Druitt et al*., 1989; *Pyle*, 1990; *Pyle and Elliott*, 2006]. Whether this difference in mechanical characteristics of the two intrusion systems reflects different petrological characteristics is beyond the scope of this paper. The association of intrusions with the two main tectonovolcanic zones in the caldera, CL and KL, is also interesting and may indicate that they play the role of ring fractures formed during the Minoan, and possibly prior caldera blowout eruptions.

Another main conclusion from this analysis is that the Santorini caldera seems to be controlled by two related feeding systems in the upper crust, controlling behavior along the KL and CL. Although a specific pattern for intrusions was deduced, the latter seem instable in space and in time, probably related to short-duration "pulses" of magma from depth, leading to composite events, like those of 1994–1999 and especially of 2011–2012. The question is whether events like those along KL have occurred in the past. Micro-earthquakes with magnitudes near or above 3 in the KL are an unsettling nuisance to the population that has only recently been felt during the 2011–2012 episode. Because no similar activity have been reported in the area since the mid-1950s, we suggest that the 2011–2012 unrest was the first (composite) pulse of deformation to produce significant microseismicity and activity in the critical segment of the KL in the last 50 years. These results are consistent with recent ideas for magma pulses in the Santorini caldera, derived from petrological data [*Parks et al*., 2012; *Druitt et al*., 2012].

11. Conclusions

The division of the 2011–2012 unrest episode into several periods independently modeled for two concurrent inflationary sources identifies deformation that enhances seismicity along the Kameni Line, and strongly suggests that Santorini is controlled by a complex and connected feeding system leading to pulses of magma injections in the upper crust. The system feeding the northern part of the caldera seems to lead to frequent, shallow, and aseismic intrusions, and perhaps to a gradual builtup of a dome. On the contrary, events along the KL, identified for the first time since the eruptions of the 1950s, seem certainly deeper, stronger, and can generate microseismicity along KL, a tectonovolcanic lineament associated with all post-Minoan eruptions.

Acknowledgments

Support by ISMOSAV (Institute for the Study and Monitoring of the Santorini Volcano), EPPO (Earthquake Planning and Protection Organization in Greece), NSF, and UNAVCO is acknowledged. Continuous GPS data retrieved from stations supported by Georgia Tech, Patras University, UNAVCO, NSF, and by Oxford University and National Technical University of Athens are available at www.geophysics.eas.gatech.edu. Campaign GPS data are summarized in www.geophysics.eas.gatech.edu. Seismological data derived from Seismological Lab of Thessaloniki University, Greece. Very constructive comments by the Associate Editor and reviews by J. Hickey and E. Fujita are much appreciated.

References

Annen, C., J.-F. Lénat, and A. Provost (2001), The long-term growth of volcanic edifices: Numerical modelling of the role of dyke intrusion and lava-flow emplacement, *J. Volcanol. Geotherm. Res.*, *105*(4), 263–289.

Blundy, J., and A. Rust (2012), Volcanology: Greek inflation circa 1600 BC, *Nature*, *482*(7383), 38–39, doi:10.1038/482038a.

Bohnhoff, M., M. Rische, T. Meier, D. Becker, G. Stavrakakis, and H.-P. Harjes (2006), Microseismic activity in the Hellenic Volcanic Arc, Greece, with emphasis on the seismotectonic setting of the Santorini–Amorgos zone, *Tectonophysics*, *423*(1–4), 17–33, doi:10.1016/j.tecto.2006.03.024.

Bond, A., and R. S. J. Sparks (1976), The Minoan eruption of Santorini, Greece, *J. Geol. Soc.*, *132*(1), 1–16, doi:10.1144/gsjgs.132.1.0001.

Cayol, V., and F. H. Cornet (1998), Effects of topography on the interpretation of the deformation field of prominent volcanoes—Application to Etna, *Geophys. Res. Lett.*, *25*(10), 1979–1982, doi:10.1029/98GL51512.

Dimitriadis, I., E. Karagianni, D. Panagiotopoulos, C. Papazachos, P. Hatzidimitriou, M. Bohnhoff, M. Rische, and T. Meier (2009), Seismicity and active tectonics at Coloumbo Reef (Aegean Sea, Greece): Monitoring an active volcano at Santorini Volcanic Center using a temporary seismic network, *Tectonophysics*, *465*(1–4), 136–149, doi:10.1016/j.tecto.2008.11.005.

Dimitriadis, I., C. Papazachos, D. Panagiotopoulos, P. Hatzidimitriou, M. Bohnhoff, M. Rische, and T. Meier (2010), P and S velocity structures of the Santorini-Coloumbo volcanic system (Aegean Sea, Greece) obtained by non-linear inversion of travel times and its tectonic implications, *J. Volcanol. Geotherm. Res.*, *195*(1), 13–30.

Dimitriadis, I. M., D. G. Panagiotopoulos, C. B. Papazachos, P. M. Hatzdimitriou, E. E. Karagianni, and I. Kane (2005), Recent seismic activity (1994–2002) of the Santorini volcano using data from local seismological network, in *The South Aegean Active Volcanic Arc Present Knowledge and Future Perspectives Milos Conferences*, Dev. Volcanol., vol. 7, edited by M. Fytikas and G. Vougioukalakis, pp. 185–203, Elsevier, Amsterdam.

Druitt, T. H., and V. Francaviglia (1992), Caldera formation on Santorini and the physiography of the islands in the late Bronze Age, *Bull. Volcanol.*, *54*(6), 484–493, doi:10.1007/BF00301394.

Druitt, T. H., R. A. Mellors, D. M. Pyle, and R. S. J. Sparks (1989), Explosive volcanism on Santorini, Greece, *Geol. Mag.*, *126*(02), 95–126, doi:10.1017/S0016756800006270.

Druitt, T. H., F. Costa, E. Deloule, M. Dungan, and B. Scaillet (2012), Decadal to monthly timescales of magma transfer and reservoir growth at a caldera volcano, *Nature*, *482*(7383), 77–80, doi:10.1038/nature10706.

Fabbro, G. N., T. H. Druitt, and S. Scaillet (2013), Evolution of the crustal magma plumbing system during the build-up to the 22-ka caldera-forming eruption of Santorini (Greece), *Bull. Volcanol.*, *75*(12), 1–22, doi:10.1007/s00445-013-0767-5.

Foumelis, M., E. Trasatti, E. Papageorgiou, S. Stramondo, and I. Parcharidis (2013), Monitoring Santorini volcano (Greece) breathing from space, *Geophys. J. Int.*, *193*(1), 161–170, doi:10.1093/gji/ggs135.

©2014. American Geophysical Union. All Rights Reserved.

Fournier, N., and L. Chardot (2012), Understanding volcano hydrothermal unrest from geodetic observations: Insights from numerical modeling and application to White Island volcano, New Zealand, *J. Geophys. Res.*, *117*, B11208, doi:10.1029/2012JB009469.
Galgana, G. A., A. V. Newman, M. W. Hamburger, and R. U. Solidum (2014), Geodetic observations and modeling of time-varying deformation at Taal Volcano, Philippines, *J. Volcanol. Geotherm. Res.*, *271*, 11–23, doi:10.1016/j.jvolgeores.2013.11.005.
Gottsmann, J., H. Rymer, and G. Berrino (2006), Unrest at the Campi Flegrei caldera (Italy): A critical evaluation of source parameters from geodetic data inversion, *J. Volcanol. Geotherm. Res.*, *150*, 132–145, doi:10.1016/j.jvolgeores.2005.07.002.
Gudmundsson, A. (2006), How local stresses control magma-chamber ruptures, dyke injections, and eruptions in composite volcanoes, *Earth Sci. Rev.*, *79*(1–2), 1–31, doi:10.1016/j.earscirev.2006.06.006.
Gudmundsson, A., L. B. Marinoni, and J. Marti (1999), Injection and arrest of dykes: Implications for volcanic hazards, *J. Volcanol. Geotherm. Res.*, *88*(1–2), 1–13, doi:10.1016/S0377-0273(98)00107-3.
Hollenstein, C. (2006), GPS deformation field and geodynamic implications for the Hellenic plate boundary region, PhD thesis, ETH Zürich, Zürich, Switzerland.
Pascal, K., J. Neuberg, and E. Rivalta (2013), On precisely modelling surface deformation due to interacting magma chambers and dykes, *Geophys. J. Int.*, *196*(1), 253–278, doi:10.1093/gji/ggt343.
Kiratzi, A. (2013), The January 2012 earthquake sequence in the Cretan Basin, south of the Hellenic Volcanic Arc: Focal mechanisms, rupture directivity and slip models, *Tectonophysics*, *586*, 160–172, doi:10.1016/j.tecto.2012.11.019.
Konstantinou, K. I., C. P. Evangelidis, W.-T. Liang, N. S. Melis, and I. Kalogeras (2013), Seismicity, Vp/Vs and shear wave anisotropy variations during the 2011 unrest at Santorini caldera, southern Aegean, *J. Volcanol. Geotherm. Res.*, *267*, 57–67, doi:10.1016/j.jvolgeores.2013.10.001.
Krizova, D., A. Kiratzi, and J. Zahradnik (2010), The 26 June 2009 Santorini Island (Cyclades) earthquake swarm in the Hellenic Volcanic Arc: Source characteristics using full moment tensor inversions, 32nd General Assembly of the ESC, Montpellier, France.
Lagios, E., V. Sakkas, F. Novali, F. Bellotti, A. Ferretti, K. Vlachou, and V. Dietrich (2013), SqueeSAR™ and GPS ground deformation monitoring of Santorini Volcano (1992–2012): Tectonic implications, *Tectonophysics*, *594*, 38–59, doi:10.1016/j.tecto.2013.03.012.
Lundgren, P., P. Berardino, M. Coltelli, G. Fornaro, R. Lanari, G. Puglisi, E. Sansosti, and M. Tesauro (2003), Coupled magma chamber inflation and sector collapse slip observed with synthetic aperture radar interferometry on Mt. Etna volcano, *J. Geophys. Res.*, *108*(B5), 2247, doi:10.1029/2001JB000657.
Masterlark, T. (2007), Magma intrusion and deformation predictions: Sensitivities to the Mogi assumptions, *J. Geophys. Res.*, *112*, B06419, doi:10.1029/2006JB004860.
McCoy, F. W., and G. Heiken (2000), Tsunami generated by the Late Bronze Age eruption of Thera (Santorini), Greece, *Pure Appl. Geophys.*, *157*(6–8), 1227–1256, doi:10.1007/s000240050024.
McTigue, D. F. (1987), Elastic stress and deformation near a finite spherical magma body: Resolution of the point source paradox, *J. Geophys. Res.*, *92*(B12), 12,931–12,940, doi:10.1029/JB092iB12p12931.
Mogi, K. (1958), Relations between the eruptions of various volcanoes and the deformations of ground surfaces around them, *Bull. Earthquake Res. Inst. Univ. Tokyo*, *36*, 99–134.
Mouslopoulou, V., V. Saltogianni, M. Gianniou, and S. Stiros (2014), Geodetic evidence for tectonic activity on the Strymon Fault System, northeast Greece, *Tectonophysics*, doi:10.1016/j.tecto.2014.07.012, in press.
Newman, A. V., et al. (2012), Recent geodetic unrest at Santorini Caldera, *Geophys. Res. Lett.*, *39*, L06309, doi:10.1029/2012GL051286.
Okada, Y. (1985), Surface deformation due to shear and tensile faults in a half space, *Bull. Seismol. Soc. Am.*, *75*(4), 1135–1154.
Papazachos, C. B., et al. (2012), Quantifying the current unrest of the Santorini volcano: Evidence from a multiparametric dataset, involving seismological, geodetic, geochemical and other geophysical data, EGU General Assembly 2012, vol. 14, EGU2012-14405, Vienna 2012.
Papoutsis, I., X. Papanikolaou, M. Floyd, K. H. Ji, C. Kontoes, D. Paradissis, and V. Zacharis (2013), Mapping inflation at Santorini volcano, Greece, using GPS and InSAR, *Geophys. Res. Lett.*, *40*, 267–272, doi:10.1029/2012GL054137.
Parks, M. M., et al. (2012), Evolution of Santorini Volcano dominated by episodic and rapid fluxes of melt from depth, *Nat. Geosci.*, *5*(10), 749–754, doi:10.1038/ngeo1562.
Poland, M., M. Hamburger, and A. Newman (2006), The changing shapes of active volcanoes: History, evolution, and future changes for volcano geodesy, *J. Volcanol. Geotherm. Res.*, *150*(1–3), 1–13.
Pyle, D. M. (1990), New estimates for the volume of the Minoan eruption, in *Thera and the Aegean World III*, vol. 2, edited by D. A. Harvy, pp. 113–21, The Thera Foundation, London.
Pyle, D. M., and J. R. Elliott (2006), Quantitative morphology, recent evolution, and future activity of the Kameni Islands volcano, Santorini, Greece, *Geosphere*, *2*(5), 253–268, doi:10.1130/GES00028.1.
Sakellariou, D., G. Rousakis, H. Sigurdsson, P. Nomikou, I. Katsenis, K. Croff Bell, and S. Carey (2012), Seismic stratigraphy of Santorini's caldera: A contribution to the understanding of the Minoan eruption, *10th Symposium on Oceanography and Fisheries*, 7–11 May 2012, Athens, Greece. [last accessed 6 Sept 2014.]
Saltogianni, V., and S. C. Stiros (2012a), Modeling the Mogi magma source centre of the Santorini (Thera) volcano, Aegean Sea, Greece, 1994–1999, based on a numerical-topological approach, *Stud. Geophys. Geod.*, *56*(4), 1037–1062, doi:10.1007/s11200-012-0408-z.
Saltogianni, V., and S. Stiros (2012b), Adjustment of highly non-linear redundant systems of equations using a numerical, topology-based approach, *J. Appl. Geod.*, *6*(3–4), 125–134, doi:10.1515/jag-2012-0018.
Saltogianni, V., and S. Stiros (2013a), Topological inversion in geodesy-based, non-linear problems in geophysics, *Comput. Geosci.*, *52*, 379–388, doi:10.1016/j.cageo.2012.11.010.
Saltogianni, V., and S. Stiros (2013b), A new algorithm for modelling simple and double Mogi magma sources in active volcanoes: Accuracy, sensitivity, limitations and implications, *Bull. Volcanol.*, *75*(10), 1–14, doi:10.1007/s00445-013-0754-x.
Seebeck, H., and A. Nicol (2009), Dike intrusion and displacement accumulation at the intersection of the Okataina Volcanic Centre and Paeroa Fault zone, Taupo Rift, New Zealand, *Tectonophysics*, *475*(3–4), 575–585, doi:10.1016/j.tecto.2009.07.009.
Sigmundsson, F., S. Hreinsdóttir, A. Hooper, T. Árnadóttir, R. Pedersen, M. J. Roberts, N. Óskarsson, et al. (2010), Intrusion triggering of the 2010 Eyjafjallajokull explosive eruption, *Nature*, *468*(7322), 426–430, doi:10.1038/nature09558.
Sigurdsson, H., et al. (2006), Marine investigations of Greece's Santorini volcanic field, *Eos Trans. AGU*, *87*(34), 337–339, doi:10.1029/2006EO340001.
Stiros, S. C., and V. Saltogianni (2014), Solution of underdetermined systems of equations with gridded a priori constraints, *SpringerPlus*, *3*(1), 1–15.
Stiros, S. C., P. Psimoulis, G. Vougioukalakis, and M. Fyticas (2010), Geodetic evidence and modeling of a slow, small-scale inflation episode in the Thera (Santorini) volcano caldera, Aegean Sea, *Tectonophysics*, *494*(3–4), 180–190, doi:10.1016/j.tecto.2010.09.015.

©2014. American Geophysical Union. All Rights Reserved.

Sturkell, E., F. Sigmundsson, H. Geirsson, H. Ólafsson, and T. Theodórsson (2008), Multiple volcano deformation sources in a post-rifting period: 1989–2005 behaviour of Krafla, Iceland constrained by levelling, tilt and GPS observations, *J. Volcanol. Geotherm. Res.*, *177*(2), 405–417, doi:10.1016/j.jvolgeores.2008.06.013.

Toda, S., R. S. Stein, and T. Sagiya (2002), Evidence from the ad 2000 Izu islands earthquake swarm that stressing rate governs seismicity, *Nature*, *419*(6902), 58–61, doi:10.1038/nature00997.

Toda, S., R. S. Stein, K. Richards-Dinger, and S. B. Bozkurt (2005), Forecasting the evolution of seismicity in southern California: Animations built on earthquake stress transfer, *J. Geophys. Res.*, *110*, B05S16, doi:10.1029/2004JB003415.

Williams, C. A., and G. Wadge (1998), The effects of topography on magma chamber deformation models: Application to Mt. Etna and radar interferometry, *Geophys. Res. Lett.*, *25*(10), 1549–1552, doi:10.1029/98GL01136.

©2014. American Geophysical Union. All Rights Reserved.